REVISION 1

Manuscript Number 8449

Word count: 8393 (incl abstract, incl references)

Nudged Elastic Band calculations of the (4H)SiX hydrogarnet type defect in Mg_2SiO_4 forsterite

Brent T. Poe*[1] and Maria Grazia Perna[2]

[1]Department of Engineering and Geology, University "G. D'Annunzio" Chieti-Pescara
Via dei Vestini 31, Chieti Scalo 66100 Italy
brent.poe@unich.it

[2]Department of Psychology, Health and Territory Sciences, University "G. D'Annunzio" Chieti-Pescara, Via dei Vestini 32, Chieti Scalo 66100 Italy
mariagrazia.perna@unich.it

*corresponding author brent.poe@unich.it (ORCID: 0000-0002-0816-0258)

This is the peer-reviewed, final accepted version for American Mineralogist, published by the Mineralogical Society of America.
The published version is subject to change. Cite as Authors (Year) Title. American Mineralogist, in press.
DOI: https://doi.org/10.2138/am-2022-8449. http://www.minsocam.org/

Abstract

First-principles calculations based on density functional theory (DFT) using the generalised gradient approximation (GGA) were performed to assess the energetic barriers separating different topological configurations of the $(4H)_{Si}^{X}$ hydrogarnet type defect in Mg_2SiO_4 forsterite with the Climbing Image Nudged Elastic Band (CI-NEB) method. Barrier heights are low (< 0.6 eV) with respect to typical activation energies observed for H-diffusion but more comparable to those for electrical conductivity of H_2O-bearing nominally anhydrous minerals. As can be expected hydrogen bonding to oxygen atoms both within the defect and belonging to adjacent tetrahedra plays a fundamental role in the stability of each configuration. Saddle points along the minimum energy path (MEP) typically correspond to the transition of one hydrogen bond breaking in order to form a new hydrogen bond such that one or more OH bonds have shifted in direction without themselves breaking. MEPs show that slightly out-of-plane torsional hopping from one configuration to another can reduce the height of the barrier. We illustrate several different reaction coordinates between symmetry equivalent pairs of configurations and non-symmetry related pairs that can result in an effective means of local charge transport by shifting the center of mass of the $(4H)^{4+}$ cluster within the defect site without proton transfer to an interstitial site. Especially at low temperatures in the absence of thermally activated processes that result in the breaking of stronger chemical bonds, these types of configurational transformation mechanisms are likely to be important contributors to the dielectric behavior of nominally anhydrous silicate minerals and also affect both electrical conductivity and electrical conductivity anisotropy when investigated by AC methods such as impedance spectroscopy. The NEB method can also be used to examine more effective charge and mass transport processes that involve the dissociation of the hydrogarnet defect

into more complex chemical species, which might involve similar hydrogen bond breaking and forming processes observed in this study along with more significant atomic displacements.

keywords: Nudged Elastic Band; Density Functional Theory; point defects; hydrous forsterite; nominally anhydrous minerals; hydrogen bonding

Introduction

Our understanding of the mineralogy and composition of the mantle is strongly based on seismological and geodynamic observations of Earth's interior combined with the comprehensive study of ultramafic rocks as well as meteorites that may bear important clues to the origin and early history of Earth's formation (McDonough and Rudnick 2019). Hydrogen, its high volatility notwithstanding, is one of the most abundant chemical elements in the Earth's crust, where it binds most favourably with oxygen to form molecular H_2O or OH^- hydroxyl groups within the crystal lattice of numerous rock-forming minerals. Even at the high pressures and temperatures at greater depths, hydrogen can be incorporated into minerals such as olivine $(Mg,Fe)_2SiO_4$ as well as several other nominally anhydrous minerals (NAMs). The presence of point defects in minerals allows for the incorporation of hydrogen, such that even at limited concentrations the overwhelming volume of such minerals in the mantle suggests a sizable H_2O reservoir comparable to the amount of liquid H_2O on Earth's surface (Ohtani 2020). Small concentrations of H_2O in the mantle are capable of influencing many geological processes, with implications for the evolution and continuing dynamics of Earth's interior. The presence of H_2O strongly influences melting temperatures and rheology and consequently plutonism, volcanism and convection (Hirth and Kohlstedt 1996; Dixon et al. 2004). In general, the presence of hydrogen in minerals affects their thermodynamic

properties and kinetic behaviour during diffusion and phase transformations (Liu 1985; Rubie and Thompson 1985).

For these reasons, several studies have focused on understanding the incorporation and diffusion of hydrogen in mantle minerals, either on natural or synthetic samples (Bell and Rossman 1992; Bai and Kohlstedt 1993; Hirth and Kohlstedt 1996; Lu and Keppler 1997; Lemaire et al. 2004; Padrón-Navarta et al. 2014; Jollands et al. 2016; Novella et al. 2017; Thoraval et al. 2019). Various studies of natural olivine samples have shown that water is distributed as OH groups at oxygen sites. Infrared (IR) absorption spectroscopy is particularly useful for obtaining chemical and structural information regarding the type of H-bearing defect species present as well as their concentrations (Libowitzky and Beran 2006; Rossman 2006; Yang and Keppler 2011). From these studies, different defect species and reaction mechanisms have been hypothesized. Bai and Kohlstedt (1993) carried out one of the first studies on hydroxyl groups in olivine, separating the observed OH bands of the IR spectrum into two main groups: group I, with phonon frequency greater than 3450 cm^{-1} and group II, with a frequency of less than 3450 cm^{-1} depending primarily on the type of point defect substitution mechanism allowing for proton incorporation. Subsequent studies have demonstrated alternative mechanisms that require trace amounts of other chemical species such as Ti or Cr, which can influence the observed or calculated OH stretching vibrational frequency (e.g. Berry et al. 2007; Gaetani et al. 2014; Tollan et al. 2017).

First-principles studies have also contributed to our understanding of H-bearing point defects in minerals. Brodholt and Refson 2000, for example, found it more energetically favorable for protonation to begin at Si vacancies compared to Mg vacancies in Mg_2SiO_4 forsterite, such that the presence of H_2O should profoundly increase Si vacancy concentrations compared to those at anhydrous conditions. Walker et al., 2006, used ab-initio

methods to calculate the phonon frequencies of various defect configurations and found that the higher frequency OH stretching vibrations (Group I as defined by Bai and Kohlstedt 1993) were associated with H-bearing defects at Si vacancies. Balan et al. (2011) also performed a study of infrared spectroscopic properties in selected defects in forsterite using first-principles calculations. A comparison of their results with experimental infrared absorption spectra indicated good agreement with their model Si_3, a hydrogarnet defect with the O2-H bond pointing away from the tetrahedral site. Umemoto et al. (2011) proposed several configurations for the hydrogarnet type defect $(4H)_{Si}^{X}$ differing slightly in total energy, all with calculated OH stretching frequencies in the Group I range. Two of their configurations had been recognized in previous studies (Brodholt and Refson 2000; Walker et al. 2006) but the other two configurations were more energetically favourable by 0.2 to 0.3 eV, the latter of which is similar to model Si_3 from Balan et al. (2011). These configurations were later investigated in the study by Xue et al., 2017, that included first-principles GIPAW calculations of ^{1}H NMR chemical shifts in good agreement with their experimental spectra of hydrous forsterite. Qin et al. 2018 calculated the relative stabilities of protonated Si vacancies and Mg vacancies as functions of pressure and temperature to emphasize the importance of configurational entropy and vibrational free energy.

Verma and Karki (2009) calculated formation and migration enthalpies of both native and protonic point defects in forsterite and its two high pressure polymorphs wadsleyite and ringwoodite. In their study the energy barrier for free proton hopping between neighbouring interstitial sites was found to be slightly greater than 1 eV, whereas the barrier between M-site vacancy and interstitial $(2H)_{Mg}^{x} \leftrightarrow H_{Mg}^{\prime} + H_{i}^{\bullet}$ was calculated to be about 2.8 eV. These energies are in fairly good agreement with experimentally observed activation energies for electrical conduction and H-diffusion, respectively, for olivine (Kohlstedt and Mackwell 1998;

Demouchy and Mackwell 2003; Wang et al. 2006; Yoshino et al. 2006; Poe et al. 2010; Dai and Karato 2014).

In the recent study by Del Vecchio et al. (2019) FTIR spectra of hydrous forsterite between room T and 600°C revealed equilibria between different H-bearing defects characterized by very low enthalpies regarded to be associated with the topological transformation from one configuration to another of the same chemical species. Their observations motivated the present study to determine the energetic barriers and minimum energy paths between different hydrogarnet defect configurations using the Nudged Elastic Band method. While reactions of this nature might not appear to involve significant atomic displacements, we examine several cases among the six different defect configurations presented here in which a shift of the (4H) barycenter makes for a compelling charge transport mechanism in hydrous silicate minerals.

Methods

The NEB method

The Nudged Elastic Band method evolved from earlier chain of states methods commonly used to explore complex potential energy surfaces in order to describe processes such as chemical reactions, transformations and mass transport (Jonsson et al. 1998). In short, the NEB method discretizes a path between two metastable atomic configurations representing the fixed endpoints (R_0 and R_N) of a reaction coordinate into a set of *i (i = N-1)* intermediate images spatially distributed by spring forces such that the total force, F_i^{neb} or simply F_i depends on the contour of the potential energy surface affecting the true forces on each individual image,

$$F_i^{neb} = F_i^{S_\parallel} + F_i^{g_\perp} \quad (1)$$

where $F_i^{S||}$ is the spring force acting upon image *i* along the local tangent and $F_i^{g\perp}$ is the true force perpendicular to the local tangent. The spring forces are applied along the tangent of the path

$$F_i^{S_\parallel} = k(|R_{i+1} - R_i| - |R_i - R_{i-1}|)T_i \quad (2)$$

where k represents the applied spring constant, which allows the true force acting on each image

$$F_i^{g_\perp} = F_i - (F_i \cdot T_i)T_i \quad (3)$$

$$F_i = -\nabla V(R_i) \quad (4)$$

to be determined such that intermediate coordinates R_i may be iteratively adjusted until the true forces are minimized. In this way, the path does not necessarily correspond to a linear interpolation of each atomic position between reactant and product, but instead finds the most economical route that crosses over a saddle point on the potential energy surface to arrive at each of the end-points following the direction of steepest descent (SD). We use a variant method, known as Climbing Image NEB (Henkelman et al. 2000), which purposely displaces one of the intermediate images such that it coincides with the atomic configuration representing the saddle point along the minimum energy path (MEP), allowing determination of the reaction's activation energy according to conventional transition state theory. Some recent uses of the NEB method range from Li tunneling in graphene (Xin et al. 2018) to reactions involving multiple spin states (Zhao et al. 2020) to the study of conformational changes in very large biomolecules (Lewis et al. 2019).

In the case of the $(4H)_{Si}^{X}$ hydrogarnet defect species, using the NEB method we provide an initial guess of the intermediate images along the reaction coordinate between two different configurations. In order to avoid significant shortening or lengthening and possibly

breaking the OH bond, we assume either a rotational or torsional movement that maintains a nearly constant OH bond length (Figure 1) throughout the entirety of the transformation. We are then able to test our assumption by examining all interatomic distances for all intermediate images after completion of the calculation.

Ab initio calculations

Calculations were performed using the Quantum Espresso suite (Giannozzi et al. 2009) with the generalized gradient approximation (GGA) for the exchange correlation energy. Two types of density functionals were used first for standard electronic structure minimization calculations in order to find suitable configurations of the hydrogarnet defect species to be used in later NEB calculations. The pw91 functional (Perdew and Wang 1992) was chosen for its noted capacity to accurately describe weaker interatomic forces such as van der Waals and hydrogen bonding interactions (Tsuzuki and Lüthi 2001) in molecular compounds, whereas the pbesol functional (Dal Corso 2010) has shown to be very effective at calculating lattice constants and the elastic behavior of densely packed solids (Csonka et al. 2009; Skelton et al. 2015). NEB calculations were limited to the pw91 functional. All calculations were performed with fixed unit cell dimensions a = 4.754, b = 10.201, c = 5.9822 angstroms (Hushur et al. 2009) as a variable cell volume is unjustified for point defect calculations. The 2 x 1 x 2 supercell, however, allows for some localized relaxation of the defect and lessens the potential of interactions between neighboring defects as the minimum defect-defect distance is nearly 10 Å (2 x *a*). Energy minimization calculations adopted a 544 eV plane wave cutoff and k-point sampling with an offset 2 x 2 x 2 grid (Monkhorst and Pack 1976). NEB calculations also adopted a 544 eV plane wave cutoff but k-point sampling was restricted to a singular gamma point and the two endpoint images were allowed to relax together with the intermediate images. Charge density cutoffs were fixed to 10 times that of

the plane wave cutoff value in all calculations. The scf convergence threshold was set at 5 x 10^{-8} a.u. (7 x 10^{-7} eV), whereas the total energy threshold was 0.001 eV and force convergence threshold was 8 x 10^{-8} N. Most of our NEB calculations consisted of 9 total images including the two endpoint images.

Because NEB calculations require two configurations representing the initial and final states of the reaction coordinate, which both must correspond to local energy minima, we first conducted a series of energy minimization calculations of the hydrogarnet species where 4 hydrogen atoms are initially placed near a vacant tetrahedral site. The first series of calculations involved a single unit cell of forsterite with the four hydrogens randomly placed within a 2.5 x 2.5 x 2.5 angstrom subcell centered at the vacant Si site. About 200 of these runs could be performed relatively quickly using minimal computational resources due to the reduced size of the model. The resulting relaxed configurations from these calculations were used as "seed" configurations, such that they could be combined with three defect-free forsterite unit cells in the form of a 2 x 1 x 2 supercell for a more time-efficient minimization. To test the possibility of bias using the seed configuration strategy, we also performed about 40 minimization runs on a 2 x 1 x 2 supercell with the four hydrogens randomly positioned near the Si vacancy.

Results

Lowest energy configurations

An overwhelming majority of the minimization calculations resulted in one of the six configurations shown in Fig. 2, which were then later investigated using the NEB method. Each configuration is two-fold degenerate, having a mirror symmetric equivalent with respect

to the *ab* plane that passes through the tetrahedral site. Each degenerate form was observed among both single cell and supercell minimization runs.

Table 1 highlights the principal characteristics of each configuration, labelled from CONF1 to CONF6 in order of increasing total energy. Each of the six configurations was observed both as the product of a seed run, as described in the Methods section, and from random (but approximate to the T vacancy) initial H positions in a 2 x 1 x 2 supercell. We note that using the seed method yielded a few important results. Firstly, as expected, many of the seed configurations were subjected to minimal topological changes upon relaxation within the larger 2 x 1 x 2 supercell. While the relative H positions of the configurations appear identical with respect to the vacant tetrahedral site, more subtle atomic displacements are allowed to disperse within the larger supercell further from the point defect. In a few cases, some novel configurations observed in the single unit cell minimization runs were not preserved after relaxation within the supercell, but instead were converted into one of the six configurations shown in Fig 2, underscoring the importance of using the larger supercells for the study of point defect species centered about a single cation vacancy.

The choice of pseudopotential greatly influences the absolute energy but has very little effect on the optimized structure when keeping the lattice parameters fixed and all other DFT functions constant (cutoffs, k-points, etc). We observe a very slight increase in the OH bond length when using the pbesol type pseudopotential (ca. 0.003 angstroms), however, this is not compensated by any change in the volume or degree of distortion of the defect tetrahedron defined by the positions of the four oxygen atoms. Most importantly, relative energy differences between different configurations compare very well for the two types of pseudopotentials used. The difference between CONF1 and CONF2 using the pbesol functional is 0.01 eV compared to 0.03 eV for the pw91 type pseudopotential. These results

provided additional confidence that the choice of pseudopotential would not likely cause significant differences in the NEB calculations, which were conducted using only the pw91 functional.

Employing the seed method allowed us to determine the effect of cell size on the total energy by comparing energies from the 2 x 1 x 2 supercell configurations to those of the single cell seed configuration + 3 times the energy of a defect-free unit cell of forsterite. Because the differences in total energy among the different configurations are small and as will be shown also the energy barriers separating configurations, it is important to be aware of how the size of the cell/supercell might influence the NEB results. Although not tested, the differences observed upon relaxation of the seed configurations within the larger 2 x 1 x 2 supercell are likely to be very large in comparison to any subsequent relaxation such as the defect-bearing 2 x 1 x 2 supercell combined with seven defect free 2 x 1 x 2 supercells relative to a fully relaxed 4 x 2 x 4 supercell on a per-unit cell basis. In other words, we assume that our model size is sufficiently large to determine meaningful minimum energy paths, and therefore energetic barrier heights, without any unnecessary consumption of additional computational resources.

Clearly evident from Table 1 is the large increase in the volume of the tetrahedral site caused by the Si ⇔ 4H substitution from ca. 2.2 $Å^3$ (no defect) to 2.9 $Å^3$ (CONF4) or as much as 3.4 $Å^3$ (CONF3). Average O-O distances increase by more than 10% from about 2.66 Å to approximately 3 Å. Among the six configurations there is no structural parameter that can be recognized as having a primary effect on the relative energy.

Our lowest energy minimization result, CONF1, is nearly identical to those observed in other studies (Balan et al. 2011; Umemoto et al. 2011; Xue et al. 2017). In this configuration, three hydrogen atoms are located along tetrahedral O-O edges but the hydrogen bonded to

O2 is pointing away from the tetrahedral site. This hydrogen, however, is slightly offset from the a-b mirror plane thus making the configuration two-fold degenerate, unlike those from both Umemoto et al. (2011) and Xue et al. (2017). Additional calculations using the same convergence criteria for both total energy and force as used in Balan et al. 2011 did not alter the results: the total energy was the same to within 0.002 eV and CONF1 remained two-fold degenerate. An additional calculation for which the H bonded to O2 was initially constrained to lie on the mirror plane removing its two-fold degeneracy and then allowed to relax caused it to revert to CONF1 as shown in Fig. 2. As will be shown below from our NEB calculations, the transition of CONF1 to its symmetry equivalent enantiomer form involves a very low energy transition state with minimal displacements of all atomic species.

Our CONF2 was also studied by Umemoto et al. (2011) and Xue et al. (2017) with a very similar total energy difference to CONF1 (0.03 eV compared to 0.022 eV (Umemoto et al. 2011) and 0 eV (Xue et al. 2017)). Our CONF3 was also observed by Xue et al. (2017), whereas CONF4 has been observed previously in several studies (Walker et al. 2006; Balan et al. 2011; Umemoto et al. 2011; Xue et al. 2017). Our CONF4 is identical to configuration 3 from Umemoto et al. (2011), with the same energy difference compared to the lowest energy configuration (0.33 eV). CONF2 and CONF4 correspond to configurations Si_4 and Si_1, respectively, from Balan et al. 2011 and the energy difference between these two configurations is the same for both studies.

We find a particularly noteworthy difference regarding the hydrogen bonded to O1 between the three most stable and three least stable configurations, in that this hydrogen stabilizes the defect when it maintains a position along either an O1-O2 or O1-O3 edge. When the O1-H bond is external to the defect tetrahedron, other hydrogens are able to

assume positions along or very near tetrahedral edges, but the relative stability of the defect is compromised.

NEB results

Upon visual examination of the configurations shown in Fig. 2 one is able to deduce the likely trajectory each atom must follow to carry out the transformation from one configuration to another. In some cases, the mechanism appears to be quite simple, with only one significant atomic displacement, such as that involving the hydrogen bonded to O1 in the conversion of CONF1 to CONF5 or the hydrogen bonded to O2 in the conversion of CONF2 to CONF3. In other cases, such as CONF3 → CONF4, we must consider the cooperative displacements of more than one atom, which increases the complexity of the calculation and requires greater attention when estimating the initial path.

The reactant-product pair in each NEB calculation performed is recognized by its marker NEB***XY***, where X and Y refer to the configurations numbered in Fig. 2 and Table 1. For example, NEB11 refers to the transformation from CONF1 to its enantiomeric equivalent configuration, whereas NEB24 refers to the transformation of CONF2 to CONF4. In the latter case there may be ambiguity because of the degeneracy of each configuration, and therefore we always refer to the lower activation energy pathway. Table 2 summarizes the results of all NEB calculations performed in this study.

NEB44 is a transformation from a configuration to its enantiomeric form that involves displacement of the hydrogen bonded to O1, which flips vertically across the a-b plane. The other three hydrogens remain nearly stationary along the three tetrahedral edges shared with O1. The energy barrier for this reaction has a height of only 0.11 eV. In Fig. 3 we illustrate the difference between the initial path, intuitively assumed to be an in-plane rotation of the OH bond between endmember configurations, and the MEP resulting from our NEB calculation,

characterized by a slight out-of-plane deviation of the initial guess that can be rationalized by examining potential hydrogen bonding interactions. The red arrows in Fig. 3 indicate the direction in which the nearest non-bonded oxygen atom lies (although not shown) for each image, and therefore the likeliest candidate as the strongest hydrogen bond along the reaction pathway. In this case, as the hydrogen moves toward the *ab* plane it remains hydrogen bonded to an oxygen associated with a nearby occupied Si site. At the transition state corresponding to the saddle point along the MEP, the O1-H bond is coincident with the *ab* mirror plane and the nearest non-bonded oxygen becomes O2, internal to the tetrahedral defect site. As it crosses the saddle point and descends toward its enantiomeric position, a new hydrogen bond is established to a different oxygen associated with an adjacent occupied Si site. As the reactant and product are symmetrically equivalent, the MEP must also be symmetric and the atomic structure representing the transition state must be non-degenerate, coinciding with a configuration at which the total energy along the path is at its maximum. The energy maximum can be associated with the breaking and reforming of hydrogen bonds without the need of breaking any stronger chemical bonds. This process can nonetheless be considered a “jump” in that the position of the hydrogen has shifted along the [001] direction after breaking and reforming hydrogen bonds. We naturally assume that any shift of the (4H) barycenter results in a corresponding shift of electronic charge distribution, but we limit this relation to a qualitative sense only. In Table 2 the total jump distance of the (4H) barycenter for each NEB calculation is listed along with specific structural characteristics of its transition state complex. In cases where we analyzed transformations between enantiomeric pairs (NEB11, NEB22, NEB33, NEB44) there is only a *c* component to the shift of the (4H) barycenter, varying from 0.2 Å (NEB11) to about 0.8 Å (NEB22).

This is the peer-reviewed, final accepted version for American Mineralogist, published by the Mineralogical Society of America.
The published version is subject to change. Cite as Authors (Year) Title. American Mineralogist, in press.
DOI: https://doi.org/10.2138/am-2022-8449. http://www.minsocam.org/

NEB22 is another transformation from a configuration to its enantiomeric form that exhibits more significant atomic displacements with an energetic barrier (0.48 eV) much greater than that observed for NEB44. The transition state structure is shown in Fig. 4 characterized by its mirror symmetry and notably short H…H distances (mean HH decreases from 2.56 to 1.89 angstroms at the transition state). Upon reaching the transition state the volume of the O_4 tetrahedron increases from 3.04 to 3.30 $Å^3$.

NEB23 resulted in a transformation having a very high energy barrier (0.59 eV). Its reaction coordinate is shown in Fig. 5a consisting of the two stable configurations (images 1 and 9, corresponding to CONF2 and CONF3, respectively) and seven intermediate images. The reaction involves the rotation of the O2-H bond from the O2-O1 tetrahedral edge to a position external to the O_4 tetrahedron while the other 3 hydrogen atoms retain their positions. Energy varies smoothly along the reaction coordinate, increasing up to the transition state located at image 5 before decreasing again. This reaction involves the largest change in O_4 tetrahedral volume V_{CONF3}-V_{CONF2}=0.37 $Å^3$, which likely contributes to its elevated activation energy.

NEB12 involves the two most energetically favorable configurations. This transformation involves the cooperative motion of different OH bonds in order to reach the saddle point along the minimum energy path. In this particular case we observe a much more complex potential energy surface. The variation in relative energy from image to image across the reaction coordinate is shown in Fig. 5b with CONF1 at far left (rel. energy = 0) and CONF2 at far right (rel. energy = 0.03 eV). Along the MEP we observe two separate transition states and a local minimum at image number 5, having a total energy and atomic positions very similar to those of CONF4. The total number of images along this reaction coordinate is likely to be too low to describe in detail the complete transformation from CONF1 to CONF2,

but we can conclude that it most likely involves passage through a metastable intermediate (CONF4) and thus combining the results from our NEB14 and NEB24 calculations would better describe this reaction's pathway.

NEB13 also involves the cooperative movement of two OH bonds. One of the hydrogens bonded to O3 located on a O3-O1 tetrahedral edge in CONF1 rotates away from the tetrahedron to an external position allowing the hydrogen bonded to O1 to switch from the O1-O2 edge to the newly vacated O1-O3 edge. The forward activation energy of 0.32 eV is in good agreement with several other calculations for which the transformation requires breaking and forming hydrogen bonds. The reverse activation energy (CONF3 -> CONF1) is only 0.19 eV owing to the higher relative energy of CONF3 with respect to CONF1. In contrast to NEB22, reaching the transition state does not involve significant shortening of HH distances nor expansion of the O_4 tetrahedral unit. We also note that the NEB13 reaction path is distinct from and slightly more economical than combining the results of NEB15 (Ea=0.35 eV) and NEB35 (reverse Ea=0.01 eV). In cases where the reverse Ea is much lower than the forward Ea the climbing image that corresponds to the transition state inevitably results very close to the terminus of the reaction coordinate (e.g. Fig. 5c image 7 of 9 in the case of NEB15).

Failed NEB trials

NEB11 can be regarded as an example that demonstrates the sensitivity limit of the method: the structural differences between the reactant-product configurations are extremely small as the hydrogen that exhibits the largest displacement moves only 0.65 Å and the overall shift of the (4H) barycenter is only 0.21 Å along the [001] direction. Although we were unable to conclusively determine its minimum energy path and activation energy due to difficulties in satisfying convergence criteria, several potential paths resulted in energy barriers < 0.01 eV to suggest more of a "speed bump" coincident with the mirror plane rather

than any well-defined saddle point. Such a low activation energy would suggest negligible change in the overall hydrogen bonding and should also be interpreted as essentially the equivalent of the non-degenerate type configuration observed by both Balan et al. (2011) and Umemoto et al. (2011), where the average position of the hydrogen even at a very low temperature would be coincident with the ab mirror plane.

NEB56 did not converge to provide a singular MEP, most likely due to the cooperative motions of three of the four H atoms needed to execute the transformation. We note, however, that NEB22 also involves the cooperative motions of three H atoms and we were successful in finding its minimum energy path. NEB33 is a case in which all four H atoms are displaced and efforts to find its MEP also proved unsuccessful. However, combining both forward and reverse reactions from NEB13 such that this reaction passes through an intermediate (CONF1) allows us to determine an upper limit to the activation energy (0.32 eV).

Discussion

Three weakly metastable configurations

The potential energy surface that delimits the numerous different configurations of the hydrogarnet $(4H)_{Si}^{X}$ defect in the forsterite lattice is clearly very complex but does not appear to contain energetic barriers greater than about 0.6 eV. Of the six configurations and their enantiomers that we investigated with the Nudged Elastic Band method, the three of highest total energy CONF4, CONF5 and CONF6 were also found to be nearly unstable in that energetic barriers of less than 0.01 eV separate them from one or more of the more stable configurations. For example, according to the results of our NEB15 calculation, the forward activation energy is 0.35 eV whereas the reverse activation energy is 0.01 eV. Similarly, low activation energies are found separating CONF5 from CONF3, CONF4 from CONF2 and

CONF6 from CONF2. While we cannot rule out the possibility of other hydrogarnet configurations that might be important in hydrous forsterite and olivine, the results of our study indicate that CONF1, CONF2 and CONF3 are considerably more likely in nature considering how their relative stabilities are influenced by temperature and pressure.

Volumetric considerations

It is particularly noteworthy that CONF1, CONF2 and CONF4 are more compact in terms of the tetrahedral volume (Table 2), which is likely to enhance their relative stabilities at higher pressures compared to the other three configurations. The NEB approach also allows us to examine how various structural characteristics of the transition state compares to those of its stable endmembers. For example, in several cases the activation energy involving a configurational transformation from higher to lower relative energy was very close to zero (rev-NEB15, rev-NEB35, rev-NEB24, see Table 2). In all of these cases we observe only a very small expansion of the O_4 tetrahedron (< 0.1 $Å^3$) at the saddle point before descending to the more stable configuration along the reaction coordinate. On the other hand, the transition state tetrahedral volume of NEB23 is 0.26 $Å^3$ greater than that for CONF2, which likely explains the high activation energy (0.59 eV) required to complete its transformation to CONF3.

Hydrogen bonding – internal vs. external

Based on our observations, electrostatic interactions between non-bonded atoms such as OH…O hydrogen bonds and H…H repulsive forces are the principal factors controlling the landscape of the potential energy surface surrounding the hydrogarnet defect. Without requiring breakage of the strong OH bond but merely its rotation about the vertex of an unoccupied tetrahedral site, this defect can assume a number of different configurational states at a very low energetic cost. Using ab initio methods Hess et al. (1988) determined the

This is the peer-reviewed, final accepted version for American Mineralogist, published by the Mineralogical Society of America.
The published version is subject to change. Cite as Authors (Year) Title. American Mineralogist, in press.
DOI: https://doi.org/10.2138/am-2022-8449. http://www.minsocam.org/

torsional energetic barriers of different H_4TO_4 molecules (T=B,C,Al,Si). In their study, the lowest energy conformation of the H_4SiO_4 molecule had S_4 symmetry with energy barriers of 0.14 and 0.43 eV at two distinct transition states each having D_{2d} symmetry. These hindered rotations are governed by H…H repulsions balanced by hydrogen bonding interactions internal to the tetrahedral site as no other oxygen atoms are present. Similar to our results for transitions between enantiomeric configurations the transition state possesses higher symmetry and the heights of the energy barriers are also in very good agreement. Umemoto et al. (2011), on the other hand, observed an inverse relationship between total energy of defect configuration and mean HH distance, whereas our results do not confirm this general trend. The ability to form and strengthen hydrogen bonds is likely to be equally if not more important to the stability of H-bearing defects in NAMs.

While it is quite normal to consider the hydrogarnet defect as simply the substitution of 4 hydrogen atoms for 1 silicon atom, it is important to consider the bonding nature of the defect environment where the oxygens that surround the tetrahedral vacancy are only associated with MgO_6 octahedra. The OH bond is therefore influenced by two types of non-bonded oxygen atoms: those belonging to occupied Si sites (external to the defect) or any of the other three oxygens associated with the defect (internal) no longer bonded to Si. The fact that (1) the O_4 unit of the defect site retains its tetrahedral symmetry rather than becoming increasingly more distorted and (2) energy barriers between different configurations are very similar to those from Hess et al. (1988) would suggest that hydrogen bonding internal to the defect plays an important role in its stability despite the counterbalance of shorter H…H distances. The absence of tetravalent Si at the center of the tetrahedral site however allows the $(4H)O_4$ tetrahedral group to expand, giving each hydrogen atom more space to pursue internal hydrogen bonds while avoiding excessive H…H repulsive forces. Examining only the

452 transition state complexes from our NEB calculations, we find that the minimum mean HH
453 distance is 1.87 angstroms (NEB44), which is only about 0.1 angstrom shorter than the mean
454 HH distance of CONF4. The importance of "internal" hydrogen bonding is also evident by our
455 observations that CONF3 has a mean HH distance nearly 0.8 angstrom longer than that of
456 CONF2 but is found to be the less stable of the two.

457 **Implications**

458 **Electrical conductivity and hydrogen diffusion**

459 Our study provides greater insight regarding the distinct difference between the
460 observed activation energies for electrical conductivity and hydrogen diffusion in hydrous
461 olivine. Among the two most stable configurations, we can reasonably conclude that CONF1
462 is essentially non-degenerate as also determined by Umemoto et al. (2011) and Xue et al.
463 (2017) but having an ill-defined potential energy surface that allows for greater lateral atomic
464 displacements of the hydrogen bonded to O2. This conclusion is supported by Balan et al.
465 2017 that found H bonded to O2 was significantly more delocalized leading to lower
466 vibrational frequencies compared to that for H bonded to O1 for their similar but non-
467 degenerate configuration. Energy barriers separating $(2H)_{Mg}$ configurations are still not known
468 but should also be investigated in order to better gauge the effects of vibrational energy and
469 configurational entropy on the relative stabilities of hydrous defects as a function of both
470 pressure and temperature (Qin et al. 2018).

471 In contrast, CONF2, which is very similar in energy to CONF1, must overcome an
472 energy barrier of 0.48 eV to transform to its enantiomeric form. This configurational
473 transformation also involves a significant displacement of the (4H) barycenter only along the
474 [001] direction, which could contribute to increasing electrical conductivity anisotropy at lower
475 temperatures in the absence of more significant atomic displacements. Poe et al. (2010)

476 measured electrical conductivities of hydrous olivine single crystals and found that the lowest
477 activation enthalpies for electrical conduction were along the [001] direction. This could also
478 explain the difference between electrical conductivity anisotropy and hydrogen diffusion
479 anisotropy in hydrous olivine, as Thoraval et al., 2019 found H-diffusion along [100] to be five
480 times faster compared to the [001] direction. It is important to note that most electrical
481 conductivity studies carried out on nominally anhydrous silicate minerals have used AC
482 impedance spectroscopy (a review of several recent studies is given by Karato 2019).
483 Frequencies generally range from 10^0 to 10^6 Hz and equivalent circuit models are required to
484 estimate the true DC conductivity. In the case of our configurational transformations involving
485 large atomic displacements but confined to the spatial limits of the defect site, a
486 corresponding electric polarization would also result from the applied AC signal as for any
487 material with dielectric properties. The defect as a whole remains charge-neutral and its
488 mobility would nonetheless be too low to reconcile H diffusivity and electrical conductivity by
489 way of the Nernst relation. Within the defect, however, if configurational transformations
490 sufficiently alter the electric polarization and they are sufficiently abundant in concentration,
491 this flipping process would be apparent in an AC impedance spectroscopic measurement and
492 possibly hinder determination of the true DC conductivity if not modelled appropriately by a
493 more accurate equivalent circuit (Rahal et al. 2018; Wang et al. 2020). Due to their higher
494 activation energies, cation vacancy and small polaron hopping should have negligible effects
495 on conductivity at low T, whereas the abundance of interstitial protons could be correlated to
496 the more dominant interconfigurational transformation of the fully protonated hydrogarnet
497 defect. While efforts have been made to arrive at a unified EC model for hydrous olivine
498 taking into account nearly all experimental data, there still remains significant uncertainty

regarding the actual mechanism of conduction for H_2O-rich olivine at moderate to low temperatures (Gardés et al. 2014).

Hydrogen diffusion in NAMs, on the other hand, requires equilibrium processes between different H-bearing defects resulting in a net mass transfer of hydrogen. In the case of hydrogarnet type defects, this would involve its dissociation into distinct chemical species such as

$$(4H)_{Si}^{X} \rightleftharpoons (3H)_{Si}^{\bullet} + H_i^{/} \quad (5)$$

a partially protonated Si vacancy and interstitial hydrogen, in which one hydrogen becomes bonded to an oxygen at an occupied Si site. These types of reactions are clearly defined by higher energy barriers associated with the breaking of stronger chemical bonds. Once such a barrier is crossed, the diffusion process can be viewed as the competition between a likely low energy barrier to return to the hydrogarnet species and another energy barrier allowing the hydrogen to further distance itself from $(3H)_{Si}^{\bullet}$. At high temperatures, this is likely to be the dominant process that controls electrical conductivity and observable by either AC or DC methods. As the interstitial hydrogen becomes increasingly more distant from the partially protonated Si vacancy, energy barriers between one interstitial site and another will become less dependent on the net balance of hydrogen bonds and H…H repulsions involving the partially protonated vacancy and increasingly more dependent on crystal structure, which can account for its anisotropy. Even for much more efficient protonic conductors such as doped $CaZrO_3$ perovskites, the rate-limiting step to hydrogen diffusion was found to have an activation energy of 0.74 eV (Kurita et al. 1995; Islam et al. 2001), significantly lower than that for H diffusion in olivine but greater than the barriers separating our hydrogarnet defect configurations.

At low temperatures, contributions from experimental studies, particularly those that use FTIR and NMR spectroscopy, are essential in order to gain a more quantitative understanding of point defect equilibria. The enthalpies associated with equilibria between H-bearing defects studied by FTIR spectroscopy between room T and 250°C are less than 0.1 eV (del Vecchio et al. 2019), which are in very good agreement with the relative energy differences among our three most stable configurations. These values, however, only place a lower limit on the activation energy of the reaction between one and another. Similar NEB studies of equilibria such as that in Equation 5 would be very helpful in distinguishing configurational transformations from actual chemical reactions involving point defects.

The Nudged Elastic Band method is ideally suited for “rare” events, and particularly for those in nominally anhydrous minerals, such as those described above and presents itself as an alternative to the more common theoretical approach of molecular dynamics. Combining a molecular dynamics approach while also incorporating metadynamics (MTD) could represent an alternative to the NEB method, although the potential energy landscape surrounding the hydrogarnet defect has been explored to the point where numerous configurations have already been proposed. A metadynamics approach would also necessitate the difficult task of choosing a proper set of order parameters, also known as collective variables, required to effectively explore the parameter space while also maintaining a strict energy resolution due to the low energy barriers separating distinct configurational species of the same point defect.

Acknowledgements

Access to supercomputing facilities were provided through a “Class C” project awarded to BTP by the Italian SuperComputing Resource Allocation (ISCRA), CINECA.

References cited

Bai, Q., and Kohlstedt, D.L. (1993) Effects of chemical environment on the solubility and incorporation mechanism for hydrogen in olivine. Physics and Chemistry of Minerals, 19, 460–471.

Balan, E., Ingrin, J., Delattre, S., Kovács, I., and Blanchard, M. (2011) Theoretical infrared spectrum of OH-defects in forsterite. European Journal of Mineralogy, 23, 285–292.

Balan, E., Blanchard, M., Lazzeri, M., and Ingrin, J. (2017) Theoretical Raman spectrum and anharmonicity of tetrahedral OH defects in hydrous forsterite. European Journal of Mineralogy, 29, 201–212.

Bell, D.R., and Rossman, G.R. (1992) The distribution of hydroxyl in garnets from the subcontinental mantle of southern Africa. Contributions to Mineralogy and Petrology, 111, 161–178.

Berry, A.J., O'Neill, H.St.C., Hermann, J., and Scott, D.R. (2007) The infrared signature of water associated with trivalent cations in olivine. Earth and Planetary Science Letters, 261, 134–142.

Brodholt, J.P., and Refson, K. (2000) An ab initio study of hydrogen in forsterite and a possible mechanism for hydrolytic weakening. Journal of Geophysical Research: Solid Earth, 105, 18977–18982.

Csonka, G.I., Perdew, J.P., Ruzsinszky, A., Philipsen, P.H.T., Lebègue, S., Paier, J., Vydrov, O.A., and Ángyán, J.G. (2009) Assessing the performance of recent density functionals for bulk solids. Physical Review B - Condensed Matter and Materials Physics, 79, 1–14.

Dai, L., and Karato, S. (2014) Influence of oxygen fugacity on the electrical conductivity of hydrous olivine: Implications for the mechanism of conduction. Physics of the Earth and Planetary Interiors, 232, 57–60.

Dal Corso, A. (2010) Projector augmented-wave method: Application to relativistic spin-density functional theory. Physical Review B - Condensed Matter and Materials Physics, 82, 1–18.

del Vecchio, A., Poe, B.T., Misiti, V., and Cestelli Guidi, M. (2019) High-temperature evolution of point defect equilibria in hydrous forsterite synthesized at 1100 °C and up to 4 GPa. Minerals, 9, 574–591.

Demouchy, S., and Mackwell, S. (2003) Water diffusion in synthetic iron-free forsterite. Physics and Chemistry of Minerals, 30, 486–494.

Dixon, J.E., Dixon, T.H., Bell, D.R., and Malservisi, R. (2004) Lateral variation in upper mantle viscosity: role of water. Earth and Planetary Science Letters, 222, 451–467.

Gaetani, G.A., O'Leary, J.A., Koga, K.T., Hauri, E.H., Rose-Koga, E.F., and Monteleone, B.D. (2014) Hydration of mantle olivine under variable water and oxygen fugacity conditions. Contributions to Mineralogy and Petrology, 167, 1–14.

Gardés, E., Gaillard, F., and Tarits, P. (2014) Toward a unified hydrous olivine electrical conductivity law. Geochemistry, Geophysics, Geosystems, 15, 4984–5000.

Giannozzi, P., Baroni, S., Bonini, N., Calandra, M., Car, R., Cavazzoni, C., Ceresoli, D., Chiarotti, G.L., Cococcioni, M., Dabo, I., and others (2009) QUANTUM ESPRESSO: a modular and open-source software project for quantum simulations of materials. Journal of Physics: Condensed Matter, 21, 395502.

589 Henkelman, G., Uberuaga, B.P., and Jónsson, H. (2000) A climbing image nudged elastic band
590 method for finding saddle points and minimum energy paths. The Journal of chemical
591 physics, 113, 9901–9904.
592 Hess, A.C., McMillan, P.F., and O'Keeffe, M. (1988) Torsional barriers and force fields in H4TO4
593 molecules and molecular ions (T = C, B, Al, Si). Journal of Physical Chemistry, 92, 1785–1791.
594 Hirth, G., and Kohlstedt, D.L. (1996) Water in the oceanic upper mantle: implications for rheology,
595 melt extraction and the evolution of the lithosphere. Earth and Planetary Science Letters,
596 144, 93–108.
597 Hushur, A., Manghnani, M., Smyth, J.R., and Nestola, F. (2009) Crystal chemistry of hydrous
598 forsterite and its vibrational properties up to 41 GPa.
599 Islam, M.S., Davies, R.A., and Gale, J.D. (2001) Proton Migration and Defect Interactions in the
600 CaZrO3 Orthorhombic Perovskite: A Quantum Mechanical Study. Chemistry of Materials, 13,
601 2049–2055.
602 Jollands, M.C., Padron-Navarta, J.A., Hermann, J., and O'Neill, H.S.C. (2016) Hydrogen diffusion in
603 Ti-doped forsterite and the preservation of metastable point defects. American Mineralogist,
604 101, 1571–1583.
605 Jonsson, H., Mills, G., and Jacobsen, K.W. (1998) Nudged elastic band method for finding minimum
606 energy paths of transitions. In B.J. Berne, G. Ciccotti, and D.F. Coker, Eds., Classical and
607 Quantum Dynamics in Condensed Phase Simulations p. 880. World Scientific.
608 Karato, S. ichiro (2019, December 1) Some remarks on hydrogen-assisted electrical conductivity
609 in olivine and other minerals. Progress in Earth and Planetary Science. Springer Berlin
610 Heidelberg.
611 Kohlstedt, D.L., and Mackwell, S.J. (1998) Diffusion of Hydrogen and Intrinsic Point Defects in
612 Olivine: . Zeitschrift für Physikalische Chemie, 207, 147–162.
613 Kurita, N., Fukatsu, N., Ito, K., and Ohashi, T. (1995) Protonic Conduction Domain of Indium-
614 Doped Calcium Zirconate. Journal of The Electrochemical Society, 142, 1552–1559.
615 Lemaire, C., Kohn, S.C., and Brooker, R.A. (2004) The effect of silica activity on the incorporation
616 mechanisms of water in synthetic forsterite: a polarised infrared spectroscopic study.
617 Contributions to Mineralogy and Petrology, 147, 48–57.
618 Lewis, K., Lindsay, S., and Li, Y. (2019) Nudged Elastic Band Study on the N-Terminal Domain
619 Conformational Pathways of Annexin A1 from a Buried State to an Exposed State. The
620 Journal of Physical Chemistry B, 123, 10163–10170.
621 Libowitzky, E., and Beran, A. (2006) The structure of hydrous species in nominally anhydrous
622 minerals: Information from polarized IR spectroscopy. Reviews in Mineralogy and
623 Geochemistry, 62, 29–52.
624 Liu, L. (1985) Effect of H2O on phase transformations of mantle silicates at high pressures and
625 temperatures. Geophysical Research Letters, 12, 530–533.
626 Lu, R., and Keppler, H. (1997) Water solubility in pyrope to 100 kbar. Contributions to
627 Mineralogy and Petrology, 129, 35–42.
628 McDonough, W.F., and Rudnick, R.L. (2019) Mineralogy and composition of the upper mantle.
629 Ultrahigh Pressure Mineralogy: Physics and Chemistry of the Earth's Deep Interior, 139–164.
630 Monkhorst, H.J., and Pack, J.D. (1976) Special points for Brillouin-zone integrations. Physical
631 Review B, 13, 5188–5192.
632 Novella, D., Jacobsen, B., Weber, P.K., Tyburczy, J.A., Ryerson, F.J., and du Frane, W.L. (2017)
633 Hydrogen self-diffusion in single crystal olivine and electrical conductivity of the Earth's
634 mantle. Scientific Reports, 7, 1–10.
635 Ohtani, E. (2020) The role of water in Earth's mantle. National Science Review, 7, 224–232.

636 Padrón-Navarta, J.A., Hermann, J., and O'Neill, H.S.C. (2014) Site-specific hydrogen diffusion rates
637 in forsterite. Earth and Planetary Science Letters, 392, 100–112.
638 Perdew, J.P., and Wang, Y. (1992) Pair-distribution function and its coupling-constant average for
639 the spin-polarized electron gas. Physical Review B, 46, 947–954.
640 Poe, B.T., Romano, C., Nestola, F., and Smyth, J.R. (2010) Electrical conductivity anisotropy of dry
641 and hydrous olivine at 8GPa. Physics of the Earth and Planetary Interiors, 181.
642 Qin, T., Wentzcovitch, R.M., Umemoto, K., Hirschmann, M.M., and Kohlstedt, D.L. (2018) Ab initio
643 study of water speciation in forsterite: Importance of the entropic effect. American
644 Mineralogist, 103, 692–699.
645 Rahal, A., Borchani, S.M., Guidara, K., and Megdiche, M. (2018) Electrical, dielectric properties and
646 study of ac electrical conduction mechanism of li0.9 □0.1 niv0.5 p0.5 o4. Royal Society Open
647 Science, 5.
648 Rossman, G.R. (2006) Analytical methods for measuring water in nominally anhydrous minerals.
649 Reviews in Mineralogy and Geochemistry, 62, 1–28.
650 Rubie, D C, and Thompson, A B (1985) Kinetics of Metamorphic Reactions at Elevated
651 Temperatures and Pressures: An Appraisal of Available Experimental Data BT -
652 Metamorphic Reactions: Kinetics, Textures, and Deformation. In Alan Bruce Thompson and
653 David C Rubie, Eds., pp. 27–79. Springer New York, New York, NY.
654 Skelton, J.M., Tiana, D., Parker, S.C., Togo, A., Tanaka, I., and Walsh, A. (2015) Influence of the
655 exchange-correlation functional on the quasi-harmonic lattice dynamics of II-VI
656 semiconductors. Journal of Chemical Physics, 143.
657 Thoraval, C., Demouchy, S., and Padrón-Navarta, J.A. (2019) Relative diffusivities of hydrous
658 defects from a partially dehydrated natural olivine. Physics and Chemistry of Minerals, 46,
659 1–13.
660 Tollan, P.M.E., Smith, R., O'Neill, H.S.C., and Hermann, J. (2017) The responses of the four main
661 substitution mechanisms of H in olivine to H 2 O activity at 1050 C and 3 GPa. Progress in
662 Earth and Planetary Science, 4, 1–20.
663 Tsuzuki, S., and Lüthi, H.P. (2001) Interaction energies of van der Waals and hydrogen bonded
664 systems calculated using density functional theory: Assessing the PW91 model. The Journal
665 of Chemical Physics, 114, 3949–3957.
666 Umemoto, K., Wentzcovitch, R.M., Hirschmann, M.M., Kohlstedt, D.L., and Withers, A.C. (2011) A
667 first-principles investigation of hydrous defects and IR frequencies in forsterite: The case for
668 Si vacancies. American Mineralogist, 96, 1475–1479.
669 Verma, A.K., and Karki, B.B. (2009) Ab initio investigations of native and protonic point defects in
670 Mg2SiO4 polymorphs under high pressure. Earth and Planetary Science Letters, 285, 140–
671 149.
672 Walker, A.M., Demouchy, S., and Wright, K. (2006) Computer modelling of the energies and
673 vibrational properties of hydroxyl groups in - and -Mg2SiO4. European Journal of
674 Mineralogy, 18, 529–543.
675 Wang, D., Mookherjee, M., Xu, Y., and Karato, S.I. (2006) The effect of water on the electrical
676 conductivity of olivine. Nature, 443, 977–980.
677 Wang, J., Gao, D., Liu, H., Xie, J., and Hu, W. (2020) Equivalent circuit modeling on defect-dipole
678 enhanced dielectric permittivity. Journal of Materials Chemistry C, 8, 13235–13243.
679 Xin, Y., Huang, A., Hu, Q., Shi, H., Wang, M., Xiao, Z., Zheng, X., Di, Z., and Chu, P.K. (2018) Barrier
680 Reduction of Lithium Ion Tunneling through Graphene with Hybrid Defects: First-Principles
681 Calculations. Advanced Theory and Simulations, 1, 1700009.

682 Xue, X., Kanzaki, M., Turner, D., and Loroch, D. (2017) Hydrogen incorporation mechanisms in
683 forsterite: New insights from 1H and 29Si NMR spectroscopy and first-principles calculation.
684 American Mineralogist, 102, 519–536.
685 Yang, X., and Keppler, H. (2011) In-situ infrared spectra of OH in olivine to 1100 C. American
686 Mineralogist, 96, 451–454.
687 Yoshino, T., Matsuzaki, T., Yamashita, S., and Katsura, T. (2006) Hydrous olivine unable to account
688 for conductivity anomaly at the top of the asthenosphere. Nature, 443, 973–976.
689 Zhao, L., Watanabe, K., Nakatani, N., Nakayama, A., Xu, X., and Hasegawa, J. (2020) Extending
690 nudged elastic band method to reaction pathways involving multiple spin states. The Journal
691 of Chemical Physics, 153, 134114.
692
693

This is the peer-reviewed, final accepted version for American Mineralogist, published by the Mineralogical Society of America.
The published version is subject to change. Cite as Authors (Year) Title. American Mineralogist, in press.
DOI: https://doi.org/10.2138/am-2022-8449. http://www.minsocam.org/

694 **Figure Captions**

695

696 Figure 1. Initial estimated pathways of two hydrogen atoms (green spheres) representing the
697 reaction coordinate of the configurational transformation of a hydrogarnet defect in the
698 forsterite lattice. In this case, the other two hydrogens (not shown) as well as all other atoms
699 in the calculation have much shorter displacements from initial to final state such that they
700 can be initially estimated by linear interpolation. However, for larger atomic displacements,
701 such as that shown at bottom left of the image, a linearly interpolated path would be highly
702 unfavorable.

703

704 Figure 2. The six lowest energy configurations of the $(4\mathrm{H})_{\mathrm{Si}}^{\mathrm{X}}$ hydrogarnet defect determined in
705 this study. The total energy increases from CONF1 to CONF6.

706

707 Figure 3. Hydrogen positions (green spheres) bonded to O1 along the minimum energy path
708 between CONF4 enantiomers. Uppermost and lowermost positions correspond to the two
709 minimum energy configurations. The small blue spheres indicate the initial guess of the
710 intermediate images assuming an in-plane rotation of the OH bond. The red arrows point
711 towards the nearest non-bonded oxygen along the path, presumably indicating the direction
712 of the strongest hydrogen bond.

713

714 Figure 4. Transition state of NEB22. The hydrogen bonded to O1 (obstructed by O1) is
715 coincident to the ab plane pointing directly towards the opposite tetrahedral face. All transition
716 states involving transformation between enantiomer pairs are non-degenerate. Along this
717 reaction coordinate, the mean HH distance reaches a minimum of 1.89 angstroms at the
718 transition state.

719

720 Figure 5. Reaction coordinates of (a) NEB23, (b) NEB12 and (c) NEB15. For NEB12 two
721 separate transition states are observed (images 3 and 6) whereas the local energy minimum
722 at image 5 is very similar in both energy and structure to CONF4. The results of this
723 calculation suggest that a more accurate description of NEB12 would be the combined results
724 from NEB14 and NEB24 in which CONF4 serves as a metastable intermediate configuration
725 along the NEB12 minimum energy path.

This is the peer-reviewed, final accepted version for American Mineralogist, published by the Mineralogical Society of America.
The published version is subject to change. Cite as Authors (Year) Title. American Mineralogist, in press.
DOI: https://doi.org/10.2138/am-2022-8449. http://www.minsocam.org/

726 **Table Captions**

727

728 **Table 1. Relative energies of the six defect configurations in a 2 x 1 x 2 supercell and**
729 **their structural characteristics.** The tetrahedral distorsion parameter is simply defined as
730 the standard deviation of the six O-O distances. Tilt angle is defined as the angle between the
731 O3-O3' tetrahedral edge and the c-axis. 1 x 1 x 1 -> 2 x 1 x 2 indicates the additional
732 stabilization observed upon relaxing each seed configuration within the 2 x 1 x 2 supercell by
733 comparing its energy to the sum of the 1 x 1 x 1 defect cell configuration + 3 unit cells of
734 defect-free forsterite.

735

736 **Table 2. Summary of Nudged Elastic Band calculations.** Three runs did not converge due
737 either to a poorly defined potential energy surface (NEB11) or the cooperative displacements
738 of three (NEB56) or four (NEB33) H atoms causing difficulty in estimating the initial path.
739 NEB12 converged but resulted in two energy barriers (see Fig. 5), suggesting that the
740 combined results of NEB14 and NEB42 would better describe its reaction.

741

742
743 Figure 1

744

745

746

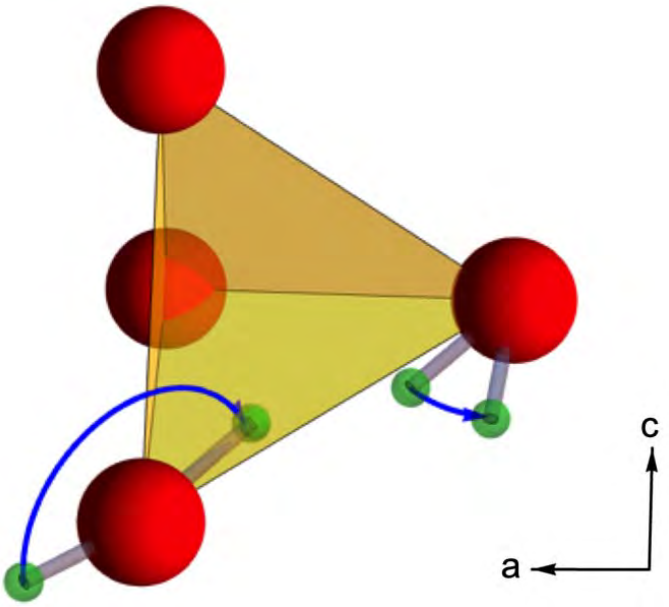

747

748

749

750

This is the peer-reviewed, final accepted version for American Mineralogist, published by the Mineralogical Society of America.
The published version is subject to change. Cite as Authors (Year) Title. American Mineralogist, in press.
DOI: https://doi.org/10.2138/am-2022-8449. http://www.minsocam.org/

Figure 2

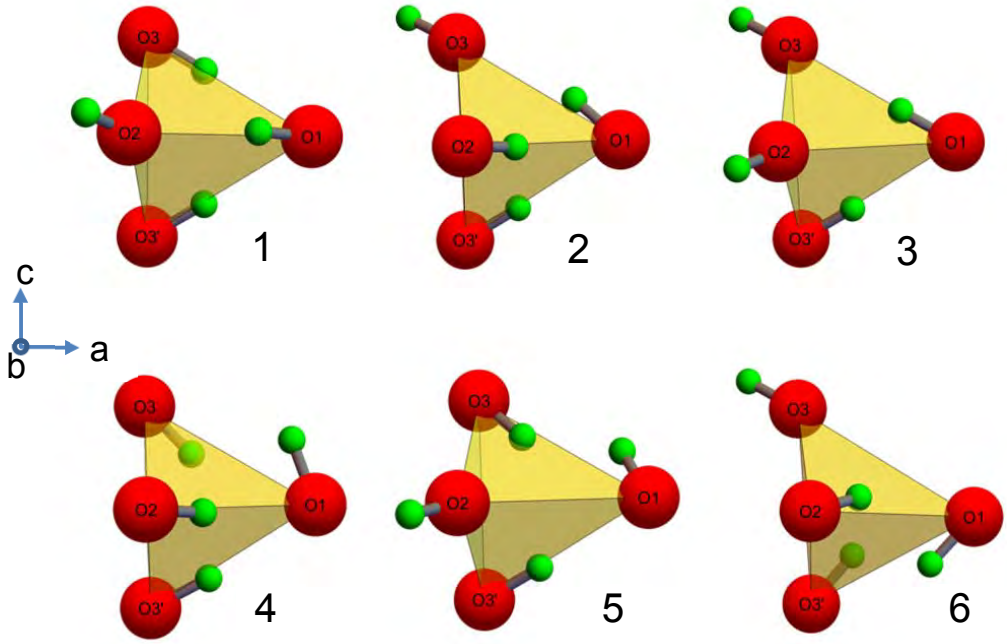

765 Figure 3

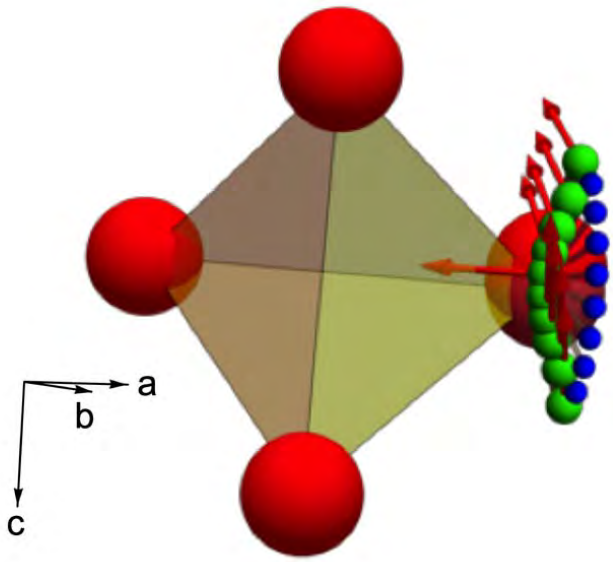

766

767

768

769

770 Figure 4

771

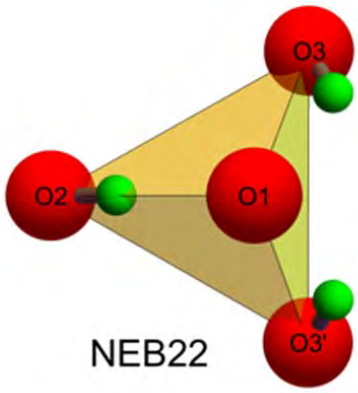

772

773

774

This is the peer-reviewed, final accepted version for American Mineralogist, published by the Mineralogical Society of America.
The published version is subject to change. Cite as Authors (Year) Title. American Mineralogist, in press.
DOI: https://doi.org/10.2138/am-2022-8449. http://www.minsocam.org/

775

776 Figure 5

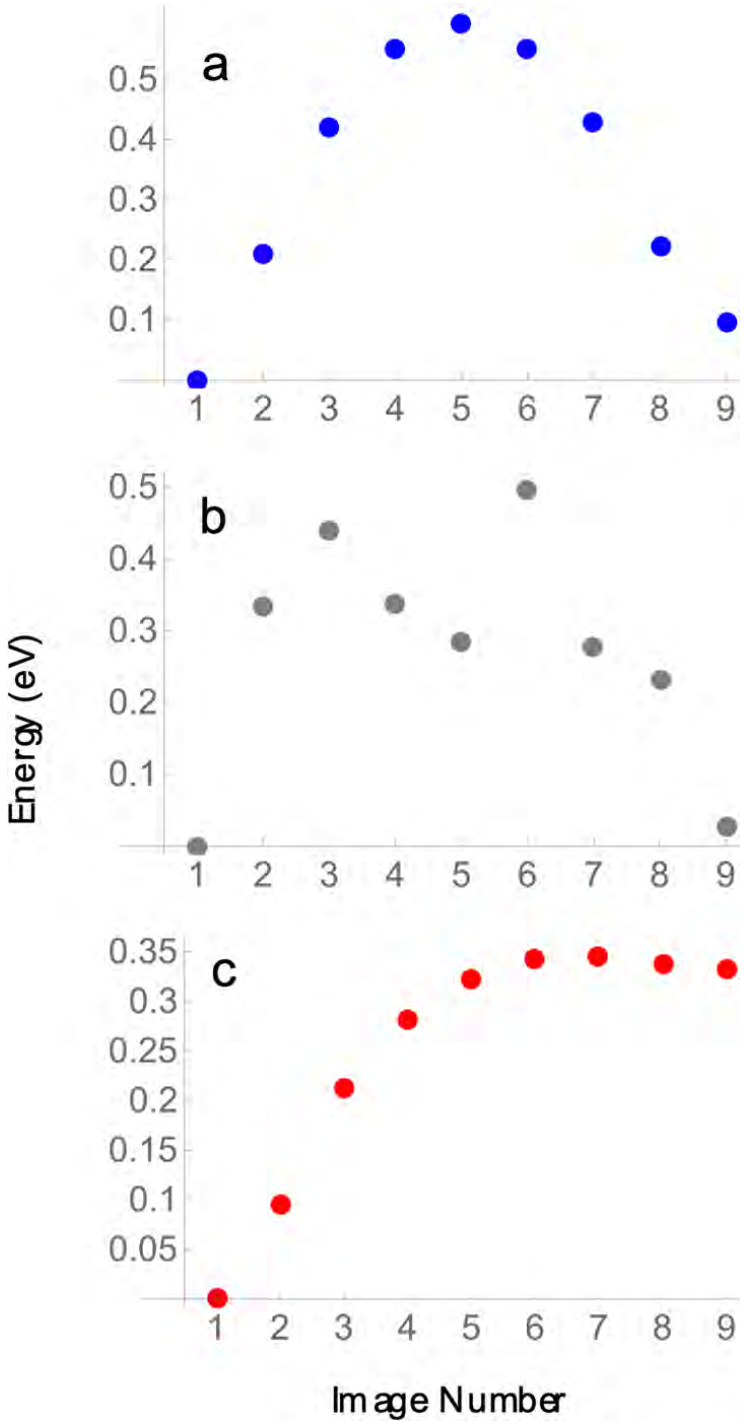

777

778

779

This is the peer-reviewed, final accepted version for American Mineralogist, published by the Mineralogical Society of America.
The published version is subject to change. Cite as Authors (Year) Title. American Mineralogist, in press.
DOI: https://doi.org/10.2138/am-2022-8449. http://www.minsocam.org/

780
781 **Table 1. Relative energies of the six defect configurations in a 2 x 1 x 2**
782 **supercell and their structural characteristics**
783

	Forsterite (no defect)	CONF1	CONF2	CONF3	CONF4	CONF5	CONF6
Relative enthalpy pw91 (eV)	---	0	0.03	0.13	0.22	0.33	0.44
Relative enthalphy pbesol (eV)	---	0	0.01	0.10	0.22	0.31	0.41
Degeneracy	---	2	2	2	2	2	2
Mean OO distance (Å)	2.662	2.971	2.944	3.070	2.906	2.992	2.990
Tetrahedral volume ($Å^3$)	2.211	3.084	2.999	3.379	2.887	3.105	3.114
Tetrahedral distortion	0.105	0.077	0.066	0.128	0.042	0.174	0.144
Tilt angle (°)	0.08	0.27	2.60	3.45	2.15	1.70	3.98
Mean OH distance (Å)	---	0.9812	0.9834	0.9817	0.9821	0.9816	0.9793
Mean HH distance (Å)	---	2.657	2.589	3.352	1.963	2.839	2.673
1 x 1 x 1 $\rightarrow$ 2 x 1 x 2 (eV)		-0.21	-0.46	-0.26	-0.19	-0.15	-0.13

784

This is the peer-reviewed, final accepted version for American Mineralogist, published by the Mineralogical Society of America.
The published version is subject to change. Cite as Authors (Year) Title. American Mineralogist, in press.
DOI: https://doi.org/10.2138/am-2022-8449. http://www.minsocam.org/

785 **Table 2. Summary of Nudged Elastic Band calculations.**

Run	Forward Activation energy (eV)	Reverse activation energy (eV)	Net 4H barycenter displacement (Å)	Transition state O_4 volume (Å^3)	Transition state O_4 distortion	Transition state O_4 tilt angle (°)	Transition state mean HH dist (Å)
NEB11	*Did not converge*		0.21				
NEB12	*CONF4 intermediate*		0.86	*See NEB14*			
NEB22	0.48	0.48	0.82	3.30	0.100	0.008	1.89
NEB13	0.32	0.19	0.68	3.19	0.187	2.91	3.11
NEB23	0.59	0.49	0.67	3.26	0.069	3.11	2.99
NEB14	0.44	0.21	0.78	2.95	0.035	0.38	2.14
NEB33	*Did not converge*		0.61				
NEB24	0.21	0.01	0.74	2.97	0.043	0.33	1.94
NEB26	0.42	0.01	0.23	3.31	0.102	3.63	2.62
NEB44	0.11	0.11	0.40	2.87	0.058	0.12	1.87
NEB46	0.53	0.32	0.62	3.01	0.093	0.99	2.25
NEB15	0.35	0.01	0.21	3.18	0.186	2.36	2.78
NEB35	0.22	0.01	0.55	3.17	0.186	2.17	2.78
NEB56	*Did not converge*		0.59				

786